Few-Layer Tellurium: Cathodic Exfoliation and Doping for Collaborative Hydrogen Evolution

*Weiran Zheng, Yong Li, Mengjie Liu, and Lawrence Yoon Suk Lee**

Dr. Weiran Zheng, Yong Li, Mengjie Liu, Prof. Lawrence Yoon Suk Lee
Department of Applied Biology and Chemical Technology and the State Key Laboratory of Chemical Biology and Drug Discovery, The Hong Kong Polytechnic University, Hung Hom, Kowloon, Hong Kong SAR, China

Prof. Lawrence Yoon Suk Lee
Research Institute for Smart Energy, The Hong Kong Polytechnic University, Hung Hom, Kowloon, Hong Kong SAR, China

E-mail: *lawrence.ys.lee@polyu.edu.hk*

Keywords: *cathodic exfoliation, tellurium, hydrogen evolution reaction, surface modification, 2D materials*

Two-dimensional tellurium is a suitable electrocatalyst support that can assist electron transport while hosting active sites, yet its production remains challenging. Herein, we present a cathodic exfoliation method that can exfoliate Te crystal directly to Te nanosheets at low potential, also enabling simultaneous transition metal doping on Te nanosheet surface. *In situ* Raman spectra and *ex situ* characterizations reveal that the cathodic exfoliation relies on the electrostatic repulsion between Te flakes covered with *in situ* generated ditelluride (Te_2^{2-}) anions. The Te_2^{2-} anions can anchor metal ions to the surface, and the doping concentration can be tuned by adjusting the concentration of metal ion in the electrolyte. The metal-doped Te nanosheets exhibit highly improved hydrogen evolution activities. In particular, Pt-doped Te outperforms polycrystalline Pt at high overpotential. A collaborative hydrogen production mechanism *via* Volmer–Heyrovsky pathway is suggested: Te_2^{2-} adsorbs protons and assists the mass transfer to adjacent Pt atoms where the protons are reduced and released as hydrogen.

1. Introduction

Hydrogen is not only the key ingredient for many fundamental processes (*e.g.,* ammonia synthesis) that support the modern society but also considered as the cleanest fuel to power our future. The production of hydrogen by means of splitting water molecules using electricity generated from sustainable sources is desired over its traditional energy-inefficient production by using diminishing fossil fuels. Pt-based electrocatalysts have demonstrated, by far, the best performance for hydrogen evolution reaction (HER).[1] Still, the pricey commercial Pt/C (platinum nanoparticles on carbon support) catalysts, with a typical Pt content between 20 and 60 wt.%,[2] restrict their large-scale application.

Two strategies are generally adopted to reduce the cost of Pt/C without sacrificing its catalytic activity: 1) by increasing the atomic utilization efficiency of Pt *via* site engineering; and 2) by replacing Pt with earth-abundant elements.[3] The engaging of single atoms or few-atom clusters as the active sites to maximize the atom exposure to electrolyte is a proven approach.[4] However, the metal sites owning high surface energy often suffer from problems such as aggregation and corrosion.[5] Therefore, the developing of electrocatalyst supports with tailored coordination sites that can immobilize metal atoms under reaction conditions while assisting electron and proton transfer is a major challenge.[6]

Two-dimensional (2D) materials with lone-pair electrons that can coordinate with metal active sites have been considered as suitable candidates that can meet the needs.[7] One noticeable advantage is that their large specific surface area enables high mass loading of active species. Moreover, the bonding between the high-energy active sites and the 2D material can affect their electronic configuration, frequently resulting in accelerated HER rates.[6, 8] Currently, common substrates such as graphdiyne,[9] metal chalcogenide,[8] and MXenes[10] are developed to offer various coordination environments on their surface to form stable bonding with active species. However, more functionalities of using 2D materials as the electrocatalyst

support, such as high electron and proton conductivities, are yet to be enabled by exploring other 2D materials.

Tellurium (Te), the fourth member of the chalcogen family, is currently under the spotlight due to the predicted and experimentally confirmed unique physical properties of its 2D form.[11] The Te structure (**Figure 1a**) features helical atomic chains arranged in parallel configuration with an intrachain distance of 2.9 Å. The interchain interaction is believed to be of the van der Waals type and can be weakened to form the 1D and 2D forms of Te, exposing abundant Te atoms to host active sites.[11d, 12] Liu *et al.* predicted that 2D Te, as a stable state, can transfer electrons isotropically at high mobility assisted by the lone-pair electron delocalization.[13] Such property makes 2D Te a possible choice as an electrocatalyst support. Besides, its ability to form strong Te–M (M = metal) interaction on its surface for site immobilization has been confirmed by various researchers.[14]

The major challenge facing the application of 2D Te as electrocatalyst support is its preparation, which typically requires a few hundred milligrams for laboratory test. Currently, the "top-down" route to produce 2D Te, or few-layer Te, mainly relies on sonication, which is time-consuming (>4h), inefficient (post-centrifugation is required to remove unexfoliated Te), and with limited scalability.[15] On the other hand, electrochemical exfoliation has demonstrated the ability to effectively exfoliate bulk crystals to their 2D form, such as graphene[16] and black phosphorus.[17] A high voltage is typically applied to a bulk material (graphene: +10 V, black phosphorus: +3 V) to enable prolonged anodic treatment. However, Te can be readily oxidized to TeO_2 at merely 0.52 V (*vs*. standard hydrogen electrode, SHE),[18] making its anodic exfoliation infeasible.

Herein, we present the cathodic exfoliation of Te crystal to Te nanosheets in alkaline solution at low applied potential (*ca*. −400 mV *vs*. reversible hydrogen electrode, RHE). *In situ* Raman spectroscopy as well as *ex situ* methods are engaged to understand the exfoliation mechanism in which the formation of ditelluride anions is the key. The cathodic treatment also

enables simultaneous transition metal doping, in the form of single/few atoms, on the surface of exfoliated Te nanosheet. Pt-doped Te nanosheet, when used as the HER electrocatalyst, outperforms polycrystalline Pt at high overpotential, suggesting the occurrence of a collaborative hydrogen production *via* Volmer–Heyrovsky pathway.

2. Results and discussion

2.1 Cathodic exfoliation

Due to the narrow electrochemical stability window of Te^0 as revealed by its Pourbaix diagram (**Figure S1**), a three-electrode system with a Hg/HgO (1.0 M KOH) reference electrode was used to enable precise potential control (**Figure 1b**). The Te crystal, fixed by an electrode holder, was dipped into the electrolyte and used as the working electrode. A graphite rod, instead of a Pt wire, was used as the counter electrode to avoid Pt dissolution and redeposition.[19] A constant-potential treatment at −1.35 V (*vs*. Hg/HgO, or −0.42 V *vs*. RHE) was performed in 1.0 M KOH aqueous solution. Upon the application of potential, a dark violet suspension is immediately observed to surround the silvery Te crystal, and the fine material released from the Te surface slowly settles to the bottom. (**Figure 1b** and **S2a**, and supporting video) The corresponding current signal (**Figure 1c**) represents the mild electroreduction of surface Te^0 to Te_2^{2-},[20] and the unique zig–zag shape of current response indicates the detachment and exposure of fresh Te^0 surface. As the exfoliated products detach from the Te crystal, the surface area of the Te crystal decreases, resulting in decreasing current signal.

After 10,000 s, the product was collected *via* centrifugation (**Figure S2b**) and washed to remove the physisorbed K^+ and OH^- species. Notably, the color of the as-prepared electrolyte changed from dark red to black after O_2 purge for 5 min, an indication of Te_2^{2-} to Te^0 oxidation by O_2. (**Figure 1d**) Redispersing the obtained powder in water leads to the appearance of small flakes floating on the water surface (**Figure S2c**), a sign of 2D material assembly. Both optical and atomic force microscopic (AFM) images (**Figure 1e**, **1f**, and **1g**) confirm the 2D morphology of product. The lateral size of the Te nanosheet (Te NS) ranges from 1 to 4 μm, which is

significantly larger than those produced by sonication method.[15] The thickness of the Te NS ranges from 7 to 10 nm.

Comparing with the total mass loss of the Te crystal (167 mg), the dry products reclaimed 95% of the Te (159 mg). Cathodic exfoliation could also be performed in an acidic electrolyte (−0.90 V *vs*. SCE in 0.5 M H_2SO_4), as evidenced by the shiny surface after amperometry (**Figures S2d** and **S2e**). However, a large amount of Te was lost in the form of H_2Te gas (loss > 30%), causing waste of materials and great health risk. The cathodic exfoliation of Te crystal in alkaline electrolyte is thus preferred.

To understand the electrochemical exfoliation, *in situ* Raman spectroscopy was coupled with the polarization process of Te crystal from −0.75 to −1.05 V (*vs*. Hg/HgO) (setup shown in **Figure S3**) and the spectra were shown in **Figure 2a**. At its pristine form, Te crystal exhibits two main Raman-active modes (as well as a weak E_1 signal), namely A_1 at 119.5 cm^{-1} and E_2 at 139.6 cm^{-1}, which are attributed to chain expansion within the basal plane and asymmetric stretching of Te atoms within the helical chains, respectively.[12] No significant changes occur until the potential reaches −0.90 V, and a new E_2 signal evolves at a higher wavenumber (141.6 cm^{-1}). At a more negative potential of −1.05 V, the A_1 peak shift becomes obvious (blueshift by 1.2 cm^{-1} to 120.7 cm^{-1}). These changes are attributed to the formation of Te NS with fewer layers, which owns Raman peaks at higher wavenumbers.[11c] A dramatic change in Te crystal's surface is captured by the corresponding optical images (**Figure 2b**), which show the silvery surface turns red at −0.91 V, and the forming of numerous small reflective flakes (white dots in the optical images). The distinctive dark red color is known to attribute to the ditelluride anion ($[Te–Te]^{2-}$ or Te_2^{2-})[18, 21] *via* direct electroreduction of Te^0 ($2Te^0 + 2e^- \rightarrow Te_2^{2-}$).[20]

The cathodic exfoliation of Te crystal, therefore, is proposed in **Scheme 1**. In an alkaline solution, as the applied potential decreases, the Te^0 atoms at the edge and plane regions (defects of the crystal) are reduced to Te_2^{2-} species first, enabling the insert of K^+ ions to interchain/interlayer locations to form KTe_2^-. The negatively charged flakes further repel each

other, causing the detachment from the bulk crystal while exposing a new surface for further reduction (**Figure 1c**). The suspension of the formed Te NS remains stable after 10 h, and the negatively charged flakes cannot be effectively collected until the neutralizing of the surface with the help of dissolved O_2, allowing the surface Te_2^{2-} species to be oxidized back to Te^0.

2.2 Simultaneous doping of metal active sites

The electrochemical production of Te_2^{2-} on the surface of Te NS provides a universal route for foreign metal ion doping *via* M–Te_2^{2-} interaction. For example, with 5 μM of Ni^{2+} and Pt^{2+} ions present in the electrolyte, Ni- and Pt-doped Te NS (denoted as Ni/Te and Pt/Te) were obtained *via* a one-step electrochemical exfoliation.

Figure 3 outlines the structural characterization of Te NS, Ni/Te, and Pt/Te. Without foreign metal ions presenting in the electrolyte, the exfoliation products are mainly large 2D nanosheets, as suggested by the TEM image in **Figure 3a**, a result that agrees with both the optical and AFM images in **Figure 1e**, **1f**, and **1g**. A well-defined lattice spacing of 3.19 Å that corresponds to the Te(101) facet (JCPDS No. 36-1452) is found across the Te NS. High-resolution TEM (HRTEM) image of the edge region of Te NS (**Figure 3b**) reveals the layer edges, as indicated by the yellow arrows. Meanwhile, the simulated Te atomic projection along the [122] axis agrees well with the observed atomic arrangement. The selected area electron diffraction (SAED) pattern of the edge region in **Figure 3c** clearly indicates the lattice arrangement of Te NS along the *c* axis.[22]

The presence of metal ions in the electrolyte changes the morphology of Te NS dramatically from large sheets to a short (Ni/Te) and a long belt (Pt/Te) (**Figure 3d** and **3e**). Such differences are most likely caused by the different coordination behaviors of different metal ions with Te_2^{2-}. **Figure S4** suggests that both Ni^{2+} and Pt^{2+} can form stable MTe_2 structures with one Te atom bonding with six M atoms. Yet, eight K^+ (from KOH electrolyte) ions bind to one Te atom to form K_2Te with the formation energy of −1.024 eV, the strongest bonding followed by $PtTe_2$ and $NiTe_2$. Therefore, it seems that the strong bonding between metal ion and Te atoms

promotes the formation of 2D Te with large lateral size. Despite the altered morphology, the same lattice spacing of Te(101) plane is widely observed in Ni/Te and Pt/Te, suggesting a dominating Te structure. No metal telluride nanoparticle structure is evident in either doped samples (HRTEM images in **Figure S5**). AFM image of the Pt/Te sample (**Figure 3f**) reveals that the long belt structure has a height between 12 and 17 nm, much smaller than their width (100~200 nm as suggested by TEM).

Comparing the X-ray diffraction (XRD) patterns before and after exfoliation (**Figure 3g**), the highly-ordered Te crystal shows a dominating signal of (100) facet and its higher index (200) and (300) planes, indicating its numerous stacking (100) planes (inset of **Figure 3g**).[23] After exfoliation, the diffraction intensities of the three peaks decrease significantly, accompanied by the appearance of a new major (101) peak and other peaks. This is clear indication of the presence of fewer Te(100) planes as well as the exposure of Te(101), Te(012), and Te(110) surfaces in Te NS. Interestingly, the (100) diffraction peak shifts by 0.4° (from 22.7° to 23.1°), indicating the occurrence of possible lattice contraction by 0.1 Å after electrochemical exfoliation. However, since the pattern of the Te crystal shows shift compared with the standard pattern of Te powder, instrumental reasons (such as tilted surface of Te crystal) cannot be ruled out. Both Ni/Te and Pt/Te show similar diffraction patterns to that of Te NS, confirming the successful exfoliation while ruling out any large-scale formation of crystalline M_xTe_y (*e.g.*, NiTe and PtTe), apart from the weak broad signal of the $NiTe_2$ (101) facet (JCPDS No. 08-0004). Similarly, the dominating Te structure is also confirmed by the Raman spectra of the three samples, shown in **Figure 3h**, which show only A_1 and E_2 vibration modes contributed by crystalline Te atoms.

The surface species of undoped and doped Te NS are analyzed by X-ray photoelectron spectroscopy (XPS, Survey spectra in **Figure S6**). All spectra show the presence of Te and O due to the inevitable oxidation of surface Te^0 to TeO_2 when exposed to air.[24] The surface atomic ratio between foreign metal and Te is 0.10:0.90 (Pt:Te) and 0.13:0.87 (Ni:Te) for Pt/Te

and Ni/Te, respectively. **Figure 4a** compares the high-resolution core-level spectra of the Te 3*d* region, featuring two groups: Te $3d_{5/2}$ and Te $3d_{3/2}$. For Te NS, the dominating species on its surface is TeO_2, as evidenced by the peaks at 576.0 and 586.4 eV, together with the minor signals contributed by the Te^0 and Te_2^{2-} species. The unoxidized anions are most likely stabilized by K^+ ions. For both Ni/Te and Pt/Te, TeO_2 remains the main species, and Te_2^{2-} is stabilized by Ni^{2+} and Pt^{2+} ions, whereas the population of Te^0 in the Pt/Te sample is much higher than that in Ni/Te or Te NS. It is thus suggested that Pt can protect Te^0 from oxidation by O_2. The Pt 4*f* region provides further insight, as shown in **Figure 4b**, that two Pt species, namely Pt^0 (69.8 at.%) and Pt^{2+}(30.2 at.%), co-exist on the Pt/Te surface. The dominating Pt^0 can be produced either through the redox with Te_2^{2-} or electrochemical reduction of adsorbed Pt^{2+} during the cathodic treatment. Similarly, co-existing Ni^0 and Ni^{2+} are evidenced by the Ni 2*p* spectrum (**Figure S7**).

The even distribution of Pt species on the Te NS surface is suggested by elemental mapping (**Figure 4c**), and high-angle annular dark-field scanning transmission electron microscopy (HAADF STEM) provides a direct observation of the Pt adatoms/clusters on the surface (**Figure 4d** and **4e**). A possible mechanism for one-step exfoliation and doping is illustrated in **Figure 3f**. Unlike **Scheme 1**, the negatively charged surface of Te NS can be stabilized by the adsorbed metal ions (Pt^{2+} in this case). Since the applied potential is lower than the reduction potential of Pt^{2+} to Pt^0 (E^o = 1.18 V), the Pt species can be reduced to Pt^0, promoting the formation of both Pt single atoms and clusters. After the discharge of Pt/Te NS, the remaining Te_2^{2-} anions can further anchor Pt^{2+}, resulting in the presence of both Pt^{2+} and Pt^0 on the Te NS surface.

2.3 Catalytic activity for hydrogen evolution

The ability of Te NS to host foreign adatoms makes it a suitable catalyst support to maximize the atomic utilization efficiency of active species, such as Pt. Its excellent electrical conductivity further enables electron transport to/from the active sites.[13a] To demonstrate this,

we studied the electrochemical hydrogen evolution reaction (HER) performance of the as-prepared M/Te (M = Ni, Pt) in an acidic electrolyte (0.5 M H_2SO_4). All samples were coated on a glassy carbon electrode (GCE) with the same tellurium mass loading of 0.12 mg cm^{-2}_{GEO} (per geometric area). The potential was corrected with the high-frequency resistance measured by impedance spectroscopy after each electrochemical experiment to offset the contact resistance.

Figure 5a shows the cyclic voltammograms (CVs) of Te NS and M/Te in an acidic solution. Within the studied potential range, Te NS shows typical capacitor behavior except for the minor reduction peak at 0.35 V (*vs*. RHE), which is attributed to the reduction of Te^{4+} species ($HTeO_3^-$ and TeO_3^{2-}) to Te_2^{2-}.[18] Unlike the featureless Ni/Te, Pt/Te exhibits a prominent oxidation signal from 0.49 V and two reduction peaks between 0.30 and 0.55 V. The oxidation and the corresponding reduction can be assigned to the redox between surface doping Pt^0 and Pt^{2+}, while the Te^{4+} to Te_2^{2-} process causes the other reduction signal. Most importantly, compared with Te NS, both Ni/Te and Pt/Te show notable reduction currents from −0.10 V (vs. RHE), indicating their ability to promote HER. **Figure 5b** and **5c** present a closer look at the HER activity of the M/Te samples, which are compared with the undoped Te NS and a polycrystalline Pt electrode (Pt_{poly}) that represents the complete coverage of Pt on the surface (θ_{Pt} = 100 %). For cross-comparison with other systems, the HER performance of the benchmarking Pt/C (20 wt.%) commercial HER electrocatalyst is also included.

The polarization curves (**Figure 5b**) suggest that Pt/C electrocatalyst, followed by Pt_{poly}, owns the lowest onset potential for HER among the studied samples, which is due to the formation of its well-known deposited H ($Pt^* + H^+ + e^- \rightarrow Pt–H$). As to Pt/Te and Ni/Te, more negative onset potentials are required at −0.06 and −0.18 V (*vs*. RHE), respectively, to drive the reaction, while Te NS shows no activity towards HER in this potential range.

The overpotential (η) values to achieve a current density of 10 mA cm^{-2}_{GEO} are 52, 161, 206, and 283 mV for Pt/C, Pt/Te, Pt_{poly}, and Ni/Te, accordingly. Notably, despite merely 10%

Pt coverage on the surface (from XPS), Pt/Te outperforms Pt_{poly} as the overpotential exceeds 142 mV. A different kinetic process is thus suggested, as revealed by the Tafel plots shown in **Figure 5c**. Two Tafel regions for HER can be identified: a low current region (2 ~ 10 mA cm^{-2}) and a high current one (10 ~ 30 mA cm^{-2}). The benchmarking Pt/C catalyst shows the fastest kinetics (23.6 mV dec^{-1}) in the low current region and slows down (141 mV dec^{-1}) as the current increases. On the contrary, Pt_{poly} exhibits a rather sluggish HER (152 mV dec^{-1}). Among the Te-based ones, Ni/Te shows the fastest overall kinetics (77.6 mV dec^{-1}) when the current (reaction rate) is relatively low, followed by Pt/Te (102 mV dec^{-1}). Once a higher overpotential is applied, the reaction rate increases, resulting in the steeper Tafel slopes for Ni/Te (171 mV dec^{-1}), Pt/C (141 mV dec^{-1}), and Pt_{poly} (163 mV dec^{-1}). Surprisingly, Pt/Te shows a reduced Tafel slope of 46.7 mV dec^{-1} at the high current region. The outperforming of Pt (Pt/C and Pt_{poly}) by MTe_2 at high overpotential has also been reported by others.[25]

To understand electrocatalytic behaviors, we need to revisit the generally accepted HER mechanism in the acidic electrolyte which involves three elementary steps[26]:

Volmer step: $H^+ + e^- \rightarrow H_{ads}$

Followed by:

Heyrovsky step: $H_{ads} + H^+ + e^- \rightarrow H_2$

or:

Tafel step: $H_{ads} + H_{ads} \rightarrow H_2$

The Volmer step, which is essential for proton adsorption, requires empty active sites and electron transfer. The subsequent discharge of H_2 is assisted by either the Heyrovsky step or the Tafel step. The simplified assumption that one (and only one) of the reactions being the rate-determining step (RDS) leads to the theoretical Tafel slopes of 120 mV dec^{-1} (the Volmer step as RDS), 40 mV dec^{-1} (the Heyrovsky step as RDS), and 30 mV dec^{-1} (the Tafel step as RDS), which help understand the mechanism.[26-27] However, deviation from these values is

widespread in practical experiments due to other factors, such as hydrogen diffusion limitation and surface structures.[28] Also, the reaction pathway and RDS vary according to the overpotential. For instance, Pt is known as the best electrocatalyst towards HER and follows a Volmer–Tafel pathway in an acidic environment. Within the studied potential window ($\eta > 100$ mV), nearly all available Pt sites are readily occupied by H_{ads}, leaving few sites accessible for subsequent Volmer step and thus making Volmer step the RDS.[26, 29] Our observation of a high Tafel slope of Pt_{poly} supports such justification.

The much smaller Tafel slope values of Ni/Te and Pt/Te in the same current region suggest a different RDS from Pt_{poly}, meaning that proton adsorption no longer limits the reaction at high overpotential for M/Te. Since the HER potential is more negative than the $Te^0 \rightarrow Te_2^{2-}$ reduction potential and Te NS demonstrates no ability to form Te–H_{ad}, it is likely that the electrostatic attraction between proton and Te_2^{2-} can assist the adsorption of H^+, resulting in changes in HER mechanism at high overpotential. Considering that the Pt adatoms are hosted by the neighboring Te atoms in the form of single atoms/few-atom clusters (**Figure 4d** and **4e**) with an atomic coverage of 10%, the discharge of H_2 through the Heyrovsky step (additional H^+ donated from Te_2^{2-}) is more likely, a conclusion that is also supported by a Tafel slope (46.7 mV dec^{-1}) similar to the ideal value of 40 mV dec^{-1}. This Volmer–Heyrovsky mechanism is consistent with previous findings for metal (di)tellurides, such as Bi_2Te_3, $CoTe_2$, and $NiTe_2$.[24, 30] Further stability test (**Figure 5d**) proves the strong interaction between Pt sites and the Te NS substrates under reaction conditions, where a stable current density of 28.9 mA cm^{-2} is maintained for 2 hours (η = 250 mV). Inductively coupled plasma atomic emission spectroscopy (ICP-OES) suggests an overall 0.75 at.% Pt after the 2-hour reaction, indicating a Pt loss of 4.4%.

Changing the concentration of metal ions in the electrolyte for cathodic exfoliation can result in different surface doping levels. For demonstration, by increasing the Pt^{2+} concentration from the previous 5 to 10, 15, and 20 μM, we obtained Pt_x/Te samples with different surface Pt

proportions (x) of 27%, 55%, and 73%, respectively. Such convenience enables us to study the impact of Pt–Te relative population on HER performance.

As expected, all Pt_x/Te samples demonstrate excellent HER activities, as suggested by the polarization curves in **Figure 6a**. All Pt_x/Te catalysts start to produce H_2 with an overpotential of *ca.* 50 mV. Increasing the surface Pt proportion from 10% to 55% significantly reduces the overpotential to achieve 10 mA cm^{-2}_{GEO} from 161 to 101 mV, which is reasonable since more Pt sites are provided. Such indicator is only 49 mV higher than the benchmarking Pt/C commercial catalyst. However, a more Pt-rich surface (x = 73%) delivers slightly worse HER performance, as indicated by the increased overpotential (124 mV). Since Pt atoms are doped on the Te NS's surface, such changes are most likely due to the intrinsic activity difference of individual sites at different surface Pt–Te ratios. Normalizing the current density with the population of Pt atoms (calculation methods shown in supporting information) can clarify the intrinsic activity. **Figure 6b** presents the overpotential-dependent turnover frequency (TOF) of H_2. Independent of Pt coverage, both $Pt_{0.27}$/Te and $Pt_{0.55}$/Te bring the highest TOF, followed by $Pt_{0.10}$/Te with a slight decrement of 11% at η = 300 mV. $Pt_{0.73}$/Te shows a much lower activity, 53% lower than that of $Pt_{0.55}$/Te. For comparison, Pt_{poly} shows the highest TOF in the low overpotential region (0 ~ 100 mV) while it is outperformed by Pt_x/Te at high overpotentials. A distinct volcano trend of the TOF with the Pt surface proportion is suggested, as illustrated by **Figure 6c**. Apparently, from low Pt coverage (10%) to medium level (55%), the normalized efficiency of Pt sites increases, while high coverage (73% and 100% in the case of Pt_{ploy}) leads to rapid decline. The most reasonable explanation is that Pt–Te sites (with an optimal atomic ratio, *ca*. 1:1 in this case) have higher HER efficiency than straight Pt sites. The theoretical relative formation energy (**Figure 6c**, data from Materials Project[31]) of Pt_xTe_{1-x} also indicates that Pt atoms can be stably fixed with surface coverage from 33% (Te_2Pt) to 50% (TePt).

The HER mechanism on Pt/Te is proposed in **Figure 6d** as collaborative hydrogen evolution based on the above analysis. For the sake of clarity, the different structural

configurations of Pt atoms on various Te sites (edges, facets, corners, *etc.*) are not considered, and a simplified model involving a Pt_xTe_{1-x} monolayer on Te NS is used here. At low overpotential (<50 mV), the Pt atoms allow proton reduction to form Pt–H_{ad} (the Volmer step). However, the long distance between individual Pt atoms hinders the subsequent Tafel step, which explains the best activity of Pt_{poly} in this region. As the overpotential increases, Te^0 species are reduced to Te_2^{2-} species, which enables them to adsorb protons *via* electrostatic interaction to form H^+–Te_2^{2-}. Similar to previous observations in metal (di)telluride,[30] the H^+–Te–Pt–H_{ad} local structure facilitates the Heyrovsky step, outperforming the HER catalyzed by Pt_{poly}. After the discharge of H_2 atoms from the Pt sites, the surrounding H^+–Te sites can provide H^+ for a rapid reduction on Pt. Such a collaborative mechanism between Pt and Te sites at high overpotential shows the best efficiency with the atomic ratio of *ca*. 1:1. The ability to adsorb proton at HER condition makes few-layer Te nanosheets significantly different from other 2D supports, especially graphene. Once the surface Te_2^{2-} species are formed, the local adsorption–transfer–reduction–release processes can be proceeded by the Te–Pt unit in a collaborative fashion, enhancing the activity of individual metal active sites.

3. Conclusion

To conclude, we have demonstrated the cathodic exfoliation of Te crystal to Te nanosheets in aqueous solution at low applied potential (*ca*. −400 mV *vs*. RHE). The *in situ* generated Te_2^{2-} species on the surface of Te nanosheets are believed to be critical for exfoliation process, and the presence of Te_2^{2-} anions also enables the doping of foreign metal atoms on the surface of the Te nanosheets through electrostatic attraction in the forms of single atom/few-atom cluster. We herein present two examples: Ni-doped and Pt-doped Te nanosheets. When used as the electrocatalyst for HER, both Ni- and Pt-doped Te nanosheets exhibit high activities. Especially, the Pt-doped one outperforms polycrystalline Pt at high current density with an optimal surface atomic ratio of 1:1 (Pt:Te). A collaborative HER mechanism of Volmer–Heyrovsky pathway involving the local Pt–Te structure is suggested: Pt mainly performs the proton

reduction/hydrogen release and the adjacent Te atoms promote the proton adsorption and transport. We believe that the unique and flexible cathodic exfoliation/doping method to produce Te and M-doped Te nanosheets offers a new route for surface modification with numerous combinations and designs of Te-based electrocatalysts.

Methods

For a typical cathodic treatment, the tellurium crystal was fixed by an electrode holder and merged into the aqueous electrolyte (1.0 M KOH). The resistance between the Te crystal and the electrode holder must be sufficiently low (<10 Ω) to allow efficient cathodic treatment. A graphite rod electrode (Union Carbide, <1 ppm impurities) and a Hg/HgO (1.0 M KOH) electrode were used as the counter and reference electrodes. No pre-experimental gas purge was needed. A constant-potential treatment at −1.35 V (*vs*. Hg/HgO, or −0.42 V *vs*. RHE) was performed for 10,000 seconds. It should be noted that the cell must remain sealed during the cathodic treatment to avoid any potential health risk from H_2Te production.

The electrolyte containing exfoliated Te products was collected after the cathodic treatment, and excessive O_2/air purge was needed to oxidize ditelluride anions. After centrifugation (13,000 rpm) and washing with DI water (3 times), the Te product was collected and dried as black powder. To avoid oxidation, the Te powder was stored in a N_2-filled container.

For the production of metal doped (Ni, Pt) Te NS, the procedure was the same as above, expect that Ni and Pt metal precursors ($Ni(NO_3)_2$ and $Pt(NO_3)_2$, Sigma-Aldrich) were added into the electrolyte.

Supporting Information

Supporting Information is available from the Wiley Online Library or from the author.

Materials and methods, Pourbaix diagram of Te, Digital photos of products, in situ Raman Spectroelectrochemistry setup, Formation energy and most stable structure of Ni-Te, Pt-Te, and K-Te system, High-resolution TEM images of metal-doped Te, XPS spectra of metal-doped Te and Ni 2*p*. (PDF)

Video of cathodic exfoliation of Te crystal (MP4)

Acknowledgements
W.Z. and Y.L. contribute equally to this work. This work was supported by the Innovation and Technology Commission of Hong Kong and the Hong Kong Polytechnic University (grant number 1-BE0Y).

Received: ((will be filled in by the editorial staff))
Revised: ((will be filled in by the editorial staff))
Published online: ((will be filled in by the editorial staff))

References

[1] a) T. F. Jaramillo, K. P. Jorgensen, J. Bonde, J. H. Nielsen, S. Horch, I. Chorkendorff, *Science* **2007**, *317*, 100-102; b) S. Trasatti, *J. Electroanal. Chem. Interfacial Electrochem.* **1972**, *39*, 163-184.

[2] B. Fang, N. K. Chaudhari, M. S. Kim, J. H. Kim, J. S. Yu, *J. Am. Chem. Soc.* **2009**, *131*, 15330-15338.

[3] I. Roger, M. A. Shipman, M. D. Symes, *Nat. Rev. Chem.* **2017**, *1*, 0003.

[4] a) D. Liu, X. Li, S. Chen, H. Yan, C. Wang, C. Wu, Y. A. Haleem, S. Duan, J. Lu, B. Ge, P. M. Ajayan, Y. Luo, J. Jiang, L. Song, *Nat. Energy* **2019**, *4*, 512-518; b) J. N. Tiwari, S. Sultan, C. W. Myung, T. Yoon, N. Li, M. Ha, A. M. Harzandi, H. J. Park, D. Y. Kim, S. S. Chandrasekaran, W. G. Lee, V. Vij, H. Kang, T. J. Shin, H. S. Shin, G. Lee, Z. Lee, K. S. Kim, *Nat. Energy* **2018**, *3*, 773-782; c) S. K. Kaiser, Z. Chen, D. Faust Akl, S. Mitchell, J. Perez-Ramirez, *Chem. Rev.* **2020**.

[5] F. D. Speck, M. T. Y. Paul, F. Ruiz-Zepeda, M. Gatalo, H. Kim, H. C. Kwon, K. J. J. Mayrhofer, M. Choi, C. H. Choi, N. Hodnik, S. Cherevko, *J. Am. Chem. Soc.* **2020**, *142*, 15496-15504.

[6] B. Lu, Q. Liu, S. Chen, *ACS Catal.* **2020**, *10*, 7584-7618.

[7] a) A. Kumar, Q. Xu, *ChemNanoMat* **2018**, *4*, 28-40; b) X. Chia, M. Pumera, *Nat. Catal.* **2018**, *1*, 909-921; c) J. Pei, J. Yang, T. Yildirim, H. Zhang, Y. Lu, *Adv. Mater.* **2019**, *31*, e1706945; d) S. Guo, Y. Zhang, Y. Ge, S. Zhang, H. Zeng, H. Zhang, *Adv. Mater.* **2019**, *31*, e1902352.

[8] P. Vancso, Z. I. Popov, J. Peto, T. Ollar, G. Dobrik, J. S. Pap, C. Hwang, P. B. Sorokin, L. Tapaszto, *ACS Energy Lett.* **2019**, *4*, 1947-1953.

[9] X. P. Yin, H. J. Wang, S. F. Tang, X. L. Lu, M. Shu, R. Si, T. B. Lu, *Angew. Chem. Int. Ed.* **2018**, *57*, 9382-9386.

[10] J. Zhang, Y. Zhao, X. Guo, C. Chen, C.-L. Dong, R.-S. Liu, C.-P. Han, Y. Li, Y. Gogotsi, G. Wang, *Nat. Catal.* **2018**, *1*, 985-992.

[11] a) L. Wu, W. Huang, Y. Wang, J. Zhao, D. Ma, Y. Xiang, J. Li, J. S. Ponraj, S. C. Dhanabalan, H. Zhang, *Adv. Funct. Mater.* **2019**, *29*, 1806346; b) J. Guo, J. Zhao, D. Huang, Y. Wang, F. Zhang, Y. Ge, Y. Song, C. Xing, D. Fan, H. Zhang, *Nanoscale* **2019**, *11*, 6235-6242; c) Y. Wang, G. Qiu, R. Wang, S. Huang, Q. Wang, Y. Liu, Y. Du, W. A. Goddard, III, M. J. Kim, X. Xu, P. D. Ye, W. Wu, *Nat. Electron.* **2018**, *1*, 228-236; d) E. J. Reed, *Nature* **2017**, *552*, 40-41.

[12] Y. Du, G. Qiu, Y. Wang, M. Si, X. Xu, W. Wu, P. D. Ye, *Nano Lett.* **2017**, *17*, 3965-3973.

[13] a) Y. Liu, W. Wu, W. A. Goddard, III, *J. Am. Chem. Soc.* **2018**, *140*, 550-553; b) W. Wu, G. Qiu, Y. Wang, R. Wang, P. Ye, *Chem. Soc. Rev.* **2018**, *47*, 7203-7212.

[14] a) L. Shi, X. H. Ren, Q. Wang, Y. X. Li, F. Ichihara, H. W. Zhang, Y. Izumi, L. Ren, W. Zhou, Y. Yang, J. H. Ye, *Small* **2020**, *16*, 2002356; b) J. Y. Xu, Z. Lian, B. Wei, Y. Li, O. Bondarchuk, N. Zhang, Z. P. Yu, A. Araujo, I. Amorim, Z. C. Wang, B. Li, L. F. Liu, *ACS Catal.* **2020**, *10*, 3571-3579.

[15] Z. Xie, C. Xing, W. Huang, T. Fan, Z. Li, J. Zhao, Y. Xiang, Z. Guo, J. Li, Z. Yang, B. Dong, J. Qu, D. Fan, H. Zhang, *Adv. Funct. Mater.* **2018**, *28*, 1705833.

[16] a) A. Ambrosi, M. Pumera, *Chem. - Eur. J.* **2016**, *22*, 153-159; b) K. Parvez, Z. S. Wu, R. Li, X. Liu, R. Graf, X. Feng, K. Mullen, *J. Am. Chem. Soc.* **2014**, *136*, 6083-6091.

[17] A. Ambrosi, Z. Sofer, M. Pumera, *Angew. Chem. Int. Ed.* **2017**, *56*, 10443-10445.

[18] M. Bouroushian, *Electrochemistry of the Chalcogens*, Springer, Berlin, Heidelberg, **2010**.

[19] R. Chen, C. Yang, W. Cai, H.-Y. Wang, J. Miao, L. Zhang, S. Chen, B. Liu, *ACS Energy Lett.* **2017**, *2*, 1070-1075.
[20] M.-J. Barbier, A.-M. De Becdelievre, J. De Becdelievre, *J. Electroanal. Chem. Interfacial Electrochem.* **1978**, *94*, 47-57.
[21] B. Gautheron, G. Tainturier, C. Degrand, *J. Am. Chem. Soc.* **1985**, *107*, 5579-5581.
[22] X.-L. Li, G.-H. Cao, C.-M. Feng, Y.-D. Li, *J. Mater. Chem.* **2004**, *14*.
[23] J. Lu, Y. Xie, F. Xu, L. Zhu, *J. Mater. Chem.* **2002**, *12*, 2755-2761.
[24] X. Chia, Z. Sofer, J. Luxa, M. Pumera, *Chem. - Eur. J.* **2017**, *23*, 11719-11726.
[25] S. Anantharaj, K. Karthick, S. Kundu, *Inorg. Chem.* **2018**, *57*, 3082-3096.
[26] B. E. Conway, B. V. Tilak, *Electrochim. Acta* **2002**, *47*, 3571-3594.
[27] Y. Li, H. Wang, L. Xie, Y. Liang, G. Hong, H. Dai, *J. Am. Chem. Soc.* **2011**, *133*, 7296-7299.
[28] W. Sheng, H. A. Gasteiger, Y. Shao-Horn, *J. Electrochem. Soc.* **2010**, *157*, B1529-B1536.
[29] J. Durst, C. Simon, F. Hasché, H. A. Gasteiger, *J. Electrochem. Soc.* **2014**, *162*, F190-F203.
[30] Q. Qu, B. Liu, J. Liang, H. Li, J. N. Wang, D. Pan, I. K. Sou, *ACS Catal.* **2020**, *10*, 2656-2666.
[31] A. Jain, G. Hautier, S. P. Ong, C. J. Moore, C. C. Fischer, K. A. Persson, G. Ceder, *Phys. Rev. B* **2011**, *84*, 045115.

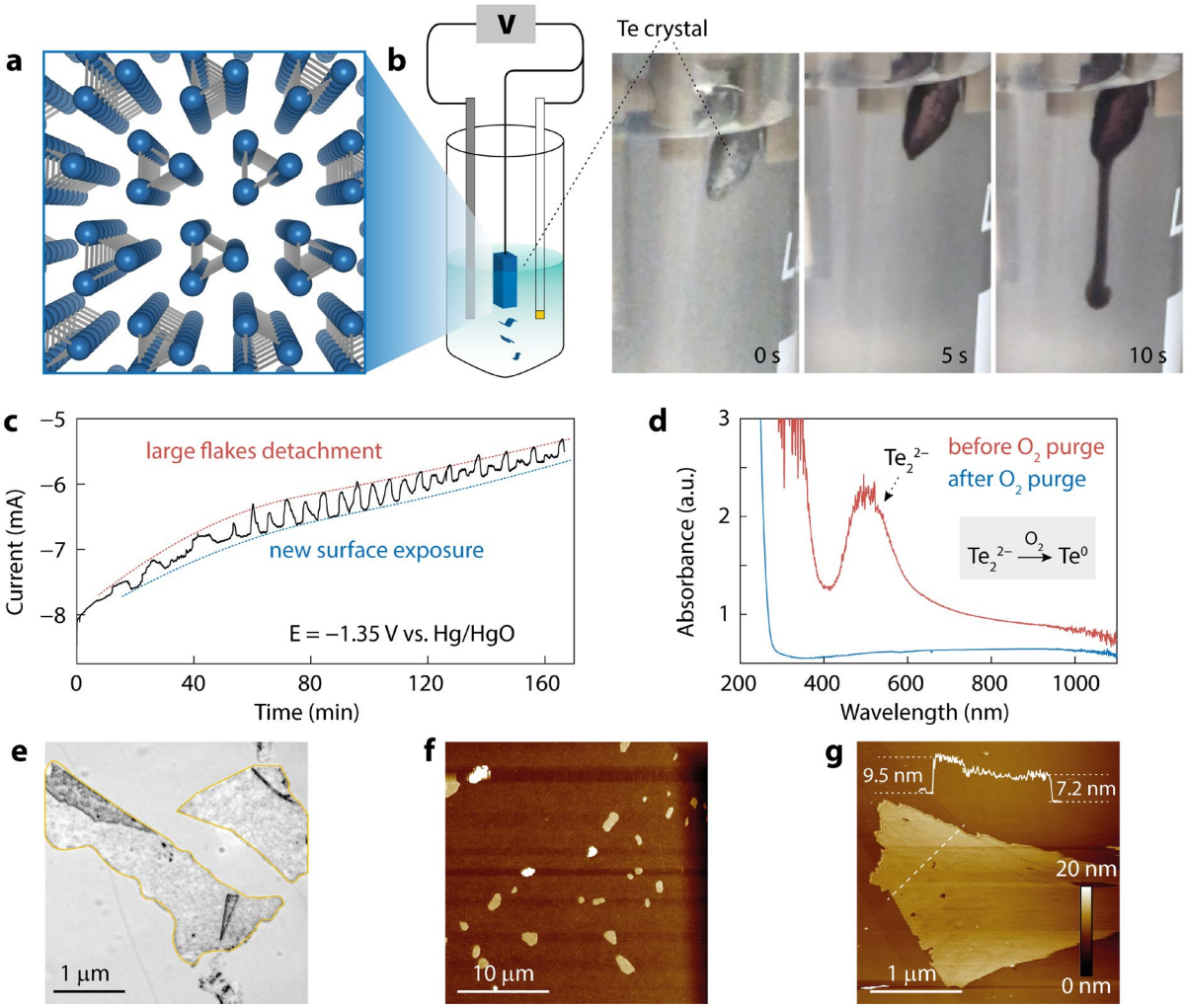

Figure 1. a) Illustration of the Te crystalline structure. b) Setup for electrochemical exfoliation of Te crystal, and the digital photos of the exfoliation process at different time: 0, 5, and 10 s. c) Corresponding amperometry curve of the exfoliation with a duration of 10,000 s at a constant potential of −1.35 V (*vs*. Hg/HgO). d) UV–vis spectra of exfoliated Te NS before and after O_2 purge. e) Optical, f, g) AFM images of Te NS on Si/SiO_2 wafer. The edges of Te NS in e) are highlighted in yellow line for clarity. Inset in g) shows the height profile of the dotted line.

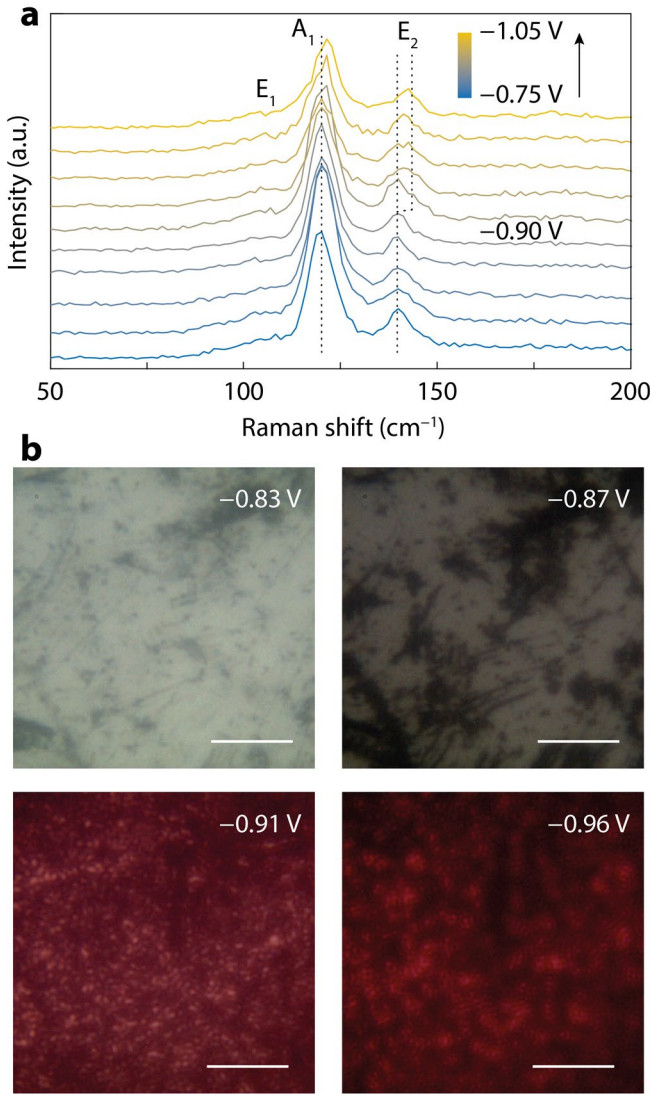

Figure 2. a) *In situ* Raman spectra accompanying the polarization from −0.75 to −1.05 V (*vs.* Hg/HgO). The laser wavelength is 785 nm. b) Optical images of the Te crystal surface at different applied potentials during Raman characterization. Scale bar indicates 20 μm.

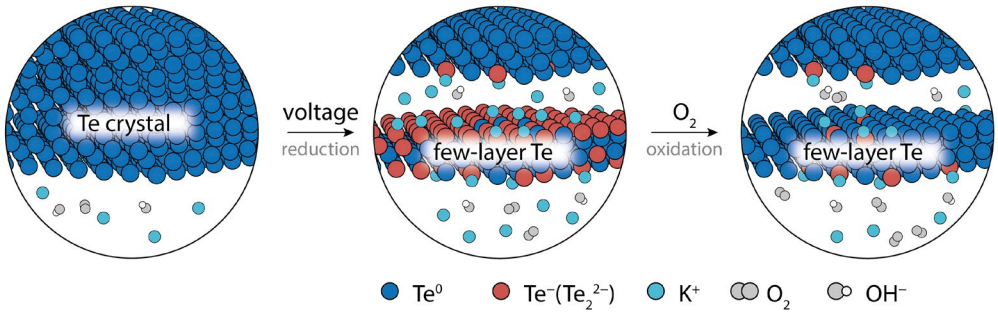

Scheme 1. Proposed mechanism of electrochemical exfoliation of Te crystal in alkaline aqueous solution.

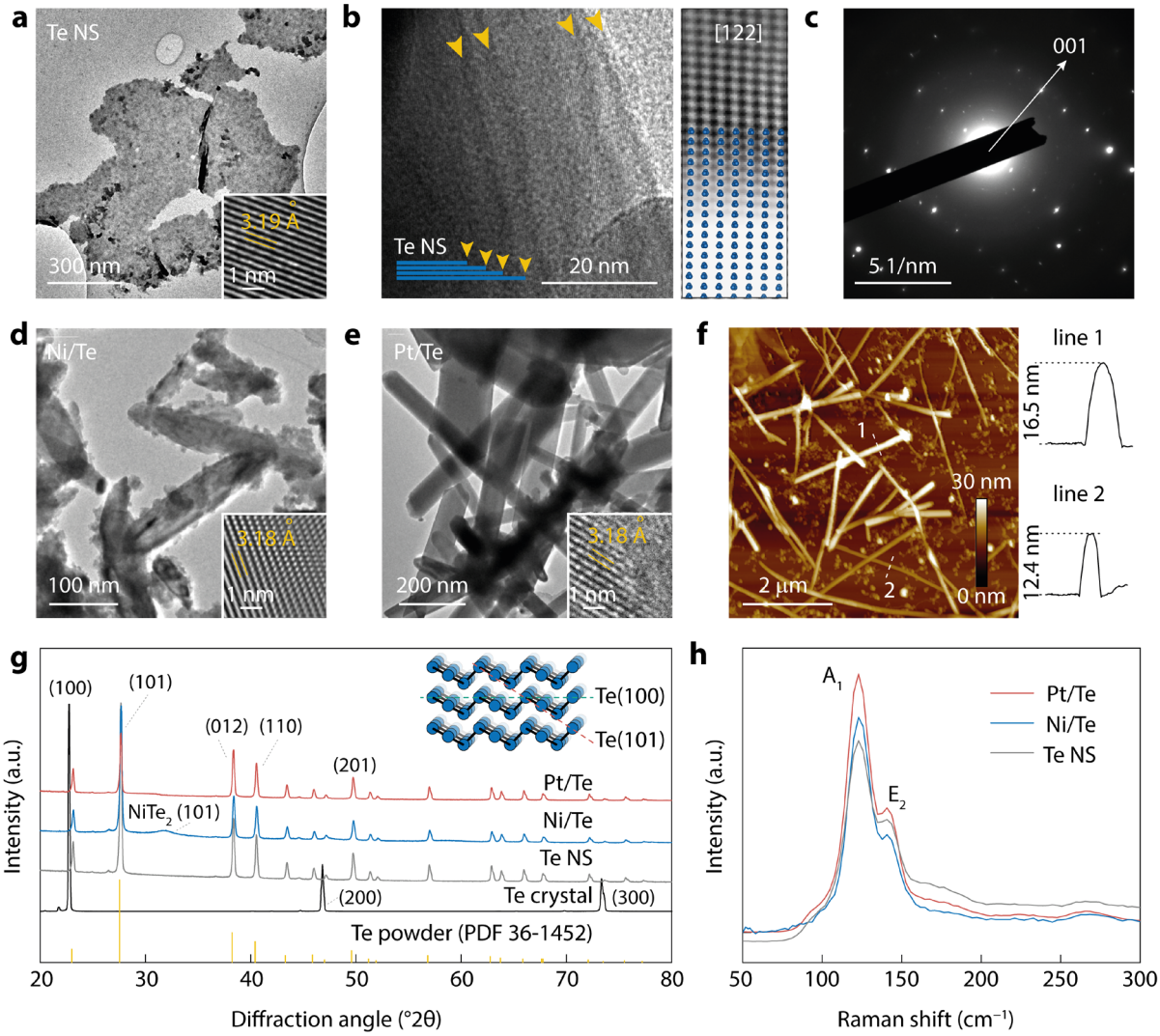

Figure 3. a) TEM and HRTEM (inset) images of as-prepared Te NS. b) TEM image of the edge region of the exfoliated Te NS. Layer edges are indicated by yellow arrows for clarity. Right: the real and corresponding simulated Te atomic projection along the [122] axis. c) SAED pattern of the region shown in b). TEM and HRTEM (inset) images of d) Ni/Te and e) Pt/Te. f) AFM image of Pt/Te supported on Si/SiO_2 wafer with the height profile of two dotted lines. g) XRD patterns of pristine Te crystal, Te NS, Ni/Te, and Pt/Te. Standard powder diffraction pattern of Te (PDF 36-1452) is indicated by the yellow lines. Inset shows the structure of Te and its Te(100) and Te(101) facets. h) Raman spectra of Te NS, Ni/Te, and Pt/Te. The laser wavelength is 785 nm.

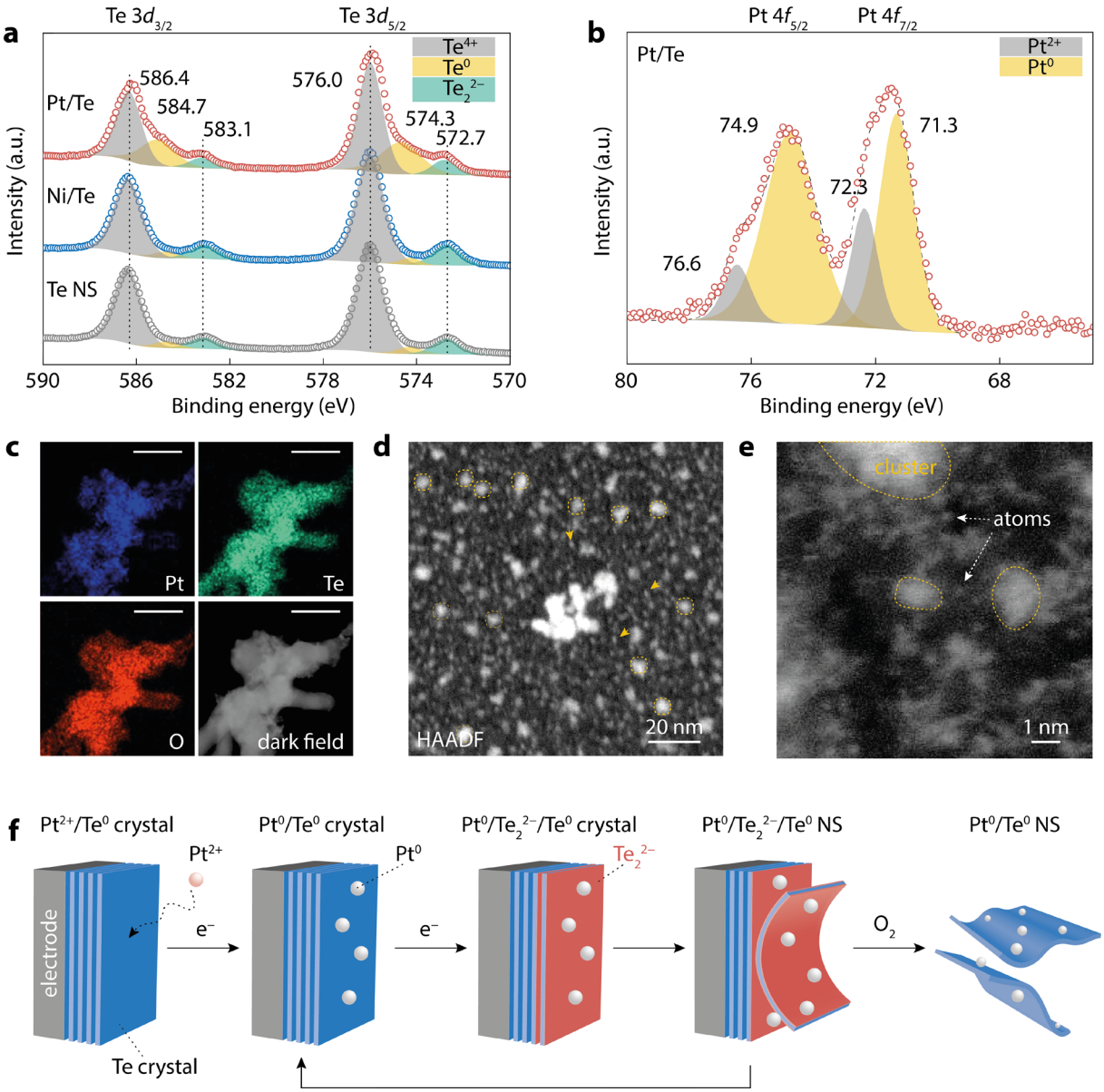

Figure 4. a) Te 3*d* XPS spectra of Te NS, Ni/Te, and Pt/Te. b) Pt 4*f* XPS spectrum of Pt/Te. A Spline Shirley background and a Gaussian–Lorentzian function (GL(30)) are used for deconvolution. c) Elemental mapping of Pt, Te, and O of Pt/Te. Scale bar indicates 200 nm. d) HAADF STEM image of Pt/Te. e) High-resolution HAADF STEM image of Pt/Te. e) High-resolution HAADF STEM image of Pt/Te. Aggregated Pt clusters and isolated Pt atoms are indicated. f) Proposed mechanism of Pt/Te production *via* a one-step exfoliation–doping process.

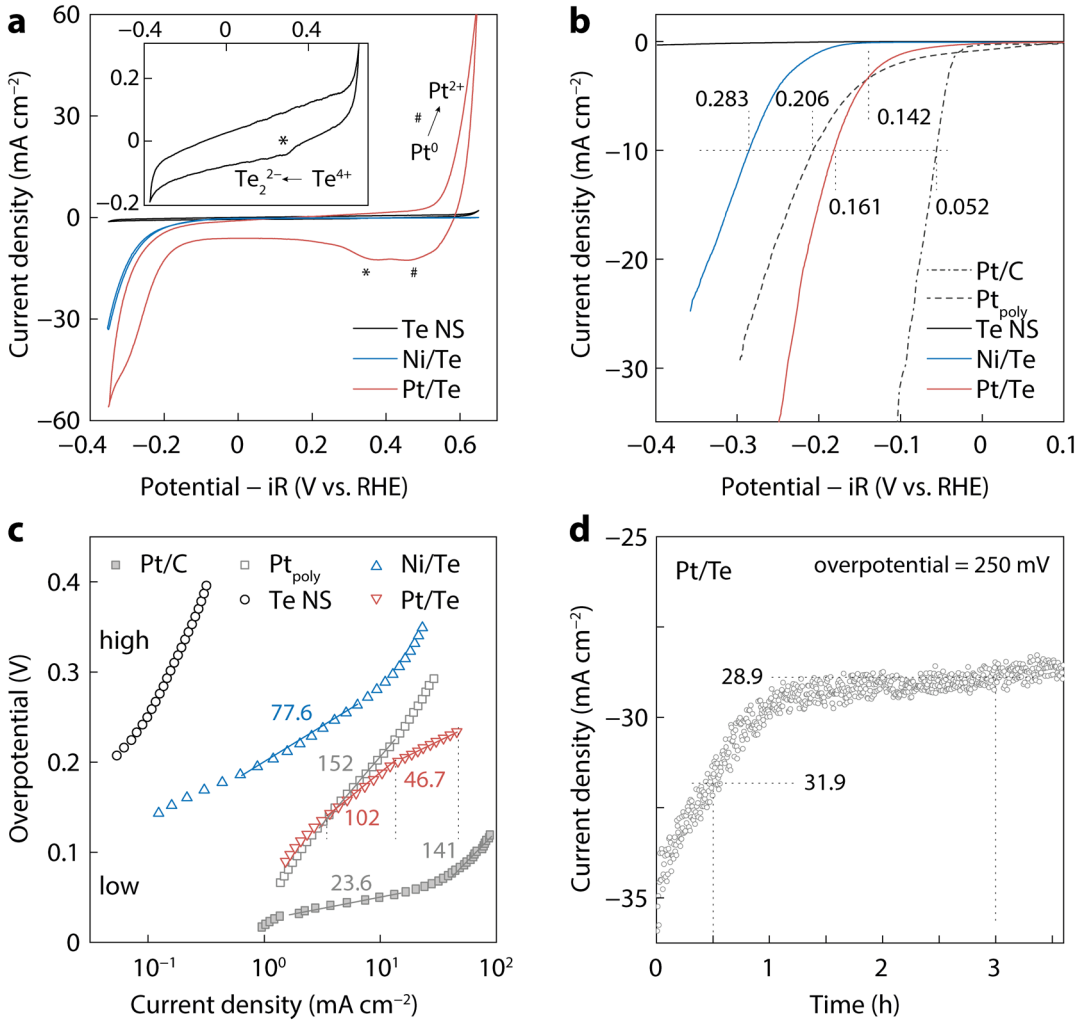

Figure 5. a) CV plots of Te NS, Ni/Te, and Pt/Te in 0.5 M H_2SO_4 measured at a scan rate of 10 mV s^{-1}. Inset shows the enlarged CV of Te NS. b) HER performance comparison between polarization curves of commercial Pt/C (20 wt.%), Pt_{poly}, Te NS, Ni/Te, and Pt/Te. Scan rate is 5 mV s^{-1}. The overpotential to achieve 10 mA cm^{-2} is marked. c) Corresponding Tafel plots of the polarization curves. The Tafel slopes (mV dec^{-1}) are marked. d) Long-term stability test of Pt/Te at an overpotential of 250 mV.

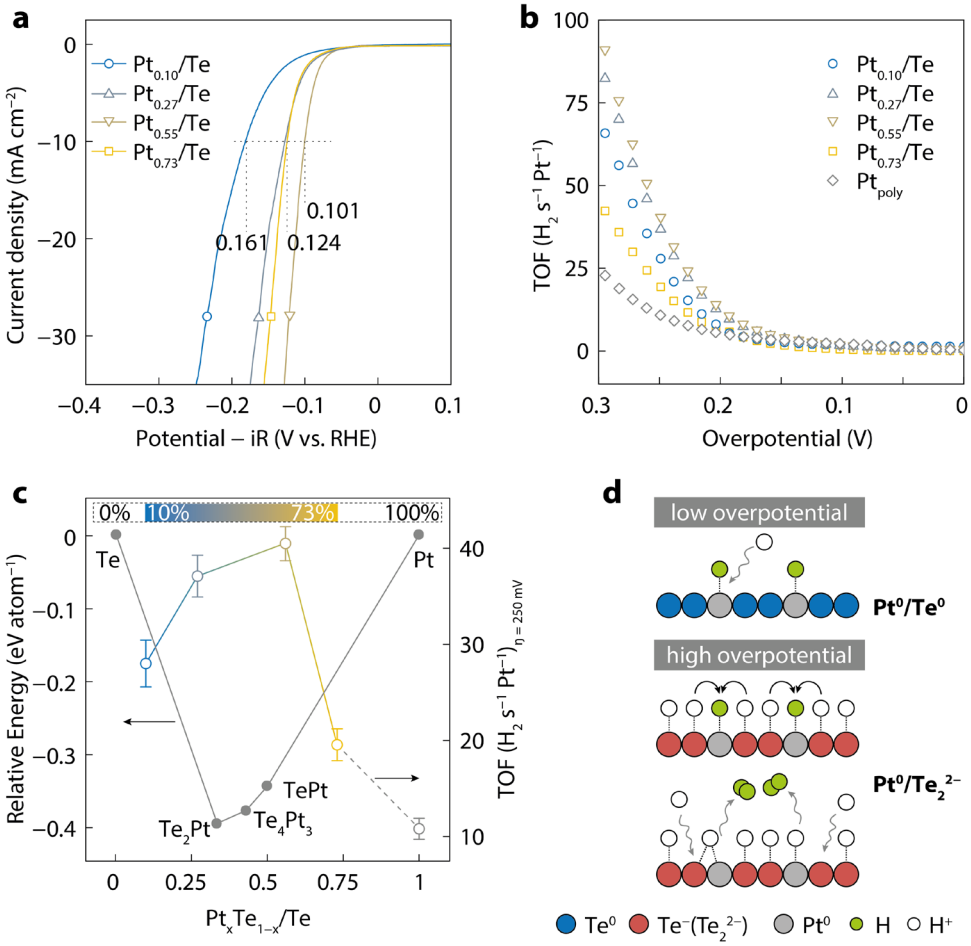

Figure 6. a) Polarization curves of Pt_x/Te in 0.5 M H_2SO_4 at a scan rate of 5 mV s^{-1}. The overpotential to achieve 10 mA cm^{-2} is marked. b) Correlation between TOF and HER overpotential for Pt_x/Te electrocatalysts. c) Relationship between relative formation energy, TOF at overpotential of 250 mV and the relative surface proportion of Pt. d) Proposed HER mechanism on Pt/Te.

Table of contents

Cathodic exfoliation of Te crystal produces its few-layer form, also enables one-step metal doping on its surface in the form of single atoms/few-atom clusters. With surface Pt coverage of *ca.* 50%, best hydrogen evolution performance is demonstrated, following the Volmer-Heyrovsky pathway, where the ditelluride anions can assist proton adsorption.

*Weiran Zheng, Yong Li, Mengjie Liu, and Lawrence Yoon Suk Lee**

Few-Layer Tellurium: Cathodic Exfoliation and Doping for Collaborative Hydrogen Evolution